The Astronomical Journal, 132:2409–2423, 2006 December


# DEEP ATLAS RADIO OBSERVATIONS OF THE CHANDRA DEEP FIELD–SOUTH/*SPITZER* WIDE-AREA INFRARED EXTRAGALACTIC FIELD

Ray P. Norris,[1] José Afonso,[2] Phil N. Appleton,[3] Brian J. Boyle,[1] Paolo Ciliegi,[4] Scott M. Croom,[5] Minh T. Huynh,[3] Carole A. Jackson,[1] Anton M. Koekemoer,[6] Carol J. Lonsdale,[7] Enno Middelberg,[1] Bahram Mobasher,[6] Seb J. Oliver,[8] Mari Polletta,[7] Brian D. Siana,[3] Ian Smail,[9] and Maxim A. Voronkov[1]

*Received 2006 June 18; accepted 2006 August 2*

## ABSTRACT

We present the first results from the Australia Telescope Large Area Survey, which consists of deep radio observations of a 3.7 deg$^2$ field surrounding the Chandra Deep Field–South, largely coincident with the infrared *Spitzer* Wide-Area Infrared Extragalactic (SWIRE) Survey. We also list cross-identifications to infrared and optical photometry data from SWIRE, and ground-based optical spectroscopy. A total of 784 radio components are identified, corresponding to 726 distinct radio sources, nearly all of which are identified with SWIRE sources. Of the radio sources with measured redshifts, most lie in the redshift range 0.5–2 and include both star-forming galaxies and active galactic nuclei. We identify a rare population of infrared-faint radio sources that are bright at radio wavelengths but are not seen in the available optical, infrared, or X-ray data. Such rare classes of sources can only be discovered in wide, deep surveys such as this.

*Key words:* catalogs — galaxies: active — galaxies: evolution — radio continuum: galaxies — surveys

*Online material:* machine-readable tables

## 1. INTRODUCTION

Large multiwavelength surveys in the last few years have proved to be powerful tools for understanding galaxy formation and evolution, particularly those that use obscuration-independent tracers of star formation and active galactic nucleus (AGN) activity, such as radio, mid-IR, and far-IR (FIR) wavelengths. However, surveys at these wavelengths have typically covered only small areas, and so not only suffer from cosmic variance but are also likely to miss intrinsically unusual objects. Those that have covered wider areas have been relatively shallow, and so may have missed the most active epochs of galaxy formation.

The *Spitzer* Wide-Area Infrared Extragalactic (SWIRE) Survey program (Lonsdale et al. 2003) has addressed these limitations by observing large (nearly 50 deg$^2$ in total) fields at mid-IR and FIR wavelengths with sufficient sensitivity to detect highly obscured, ultraluminous infrared galaxies (ULIRGs) at $z \gg 1$. SWIRE's goal is to trace the evolution of dusty, star-forming galaxies, evolved stellar populations, and AGNs from redshifts $z \sim 3$, when the universe was 2 Gyr old, to the present day.

Over the last 2 years, we have conducted the Australia Telescope Large Area Survey (ATLAS) of the Chandra Deep Field–South (CDF-S) and European Large Area *ISO* Survey–South 1 (ELAIS-S1) regions, with the aim of producing the widest (6 deg$^2$) deep (10–15 $\mu$Jy rms) radio survey ever attempted. The surveyed areas have been chosen to overlap the SWIRE areas as far as practicable, so that infrared and optical data are available for most of the radio objects. They also encompass the well-studied Great Observatories Origins Deep Survey (GOODS) field in the CDF-S (Giavalisco et al. 2004).

The broad scientific goals of this multiwavelength survey are to understand the formation and evolution of galaxies in the early universe. The radio observations are complementary to the *Spitzer Space Telescope* observations in being able to detect radio AGNs in even the most obscured galaxies, and provide additional information on the spectral energy distribution (SED) of the galaxies. Galaxies powered by star formation are expected to follow the radio-FIR correlation, while departure from this correlation is a strong indicator of an AGN.

Surveys of radio sources with flux densities greater than 1 mJy are typically dominated by AGNs, but source count statistics suggest the presence at submillijansky levels of another population (Condon 1984; Windhorst et al. 1985; Hopkins et al. 2003), which has been attributed to star-forming galaxies (e.g., Windhorst et al. 1985; Georgakakis et al. 1999; Afonso et al. 2005). However, Chapman et al. (2003b) show that many of these weaker galaxies have relatively high redshifts ($z > 1$) and luminosities ($L_{20\,\mathrm{cm}} > 10^{23}$ W Hz$^{-1}$). It is not clear whether this increased luminosity is caused by abnormally high star formation rates, such as those found in ULIRGs, or is the result of an AGN, possibly embedded within a star-forming galaxy.

There have been a number of very important deep radio surveys (e.g., Condon et al. 2003; Hopkins et al. 2003) that have produced valuable data on radio source statistics, but the potential power of these surveys is often hampered by inadequate data at other wavelengths. ATLAS is specifically targeted on wide areas that

[1] CSIRO Australia Telescope, CSIRO Radiophysics Laboratory, P.O. Box 76, Epping, NSW 1710, Australia; ray.norris@csiro.au.
[2] Observatório Astronómico de Lisboa, Faculdade de Ciências, Universidade de Lisboa, Tapada da Ajuda, 1349-018 Lisbon, Portugal; and Centro de Astronomia e Astrofísica da Universidade de Lisboa, 1349-018 Lisbon, Portugal.
[3] Spitzer Science Center, California Institute of Technology, MS 220-6, Pasadena, CA 91125.
[4] INAF, Osservatorio Astronomico di Bologna, Via Ranzani 1, I-40127 Bologna, Italy.
[5] Anglo-Australian Observatory, P.O. Box 296, Epping, NSW 1710, Australia.
[6] Space Telescope Science Institute, 3700 San Martin Drive, Baltimore, MD 21218.
[7] Center for Astrophysics and Space Sciences, University of California at San Diego, 9500 Gilman Drive, La Jolla, CA 92093-0424.
[8] Astronomy Centre, CPES, University of Sussex, Falmer, Brighton BN1 9QJ, UK.
[9] Institute for Computational Cosmology, Durham University, South Road, Durham DH1 3LE, UK.

are, or will be, well studied at other wavelengths. It is thus uniquely capable of testing the alternative hypotheses, as we have a large number of galaxies with extensive radio, infrared, and optical data (and in some cases deep X-ray data), and ATLAS should prove pivotal to understanding these objects.

Radio AGNs in the local universe are typically divided into radio-loud objects (e.g., radio quasars, radio galaxies), whose radio luminosity is generally $>10^{24}$ W Hz$^{-1}$, and radio-quiet objects (e.g., Seyfert and normal galaxies). It is not yet clear whether this classification is relevant to the early universe, where we find, for example, double and triple radio sources that resemble classical radio-loud sources, but whose radio luminosity is significantly lower. Unlike the well-studied objects in the local universe, we do not yet understand the evolution of radio sources in the early universe. For example, Magorrian et al. (1998) have shown that in the local universe the mass of the supermassive black hole in a galaxy is related to that of the bulge of the galaxy. We do not know whether this is true in the early universe, nor how it is related to the star formation rate. Particularly interesting are those cases in which the radio source lies buried within a host galaxy whose optical/infrared spectrum or SED appears to be that of a star-forming galaxy. Understanding the relationship between the AGN activity and the star-forming activity in these galaxies is a primary goal of this project.

Obscured activity may be the dominant contributor to galaxy luminosity at high redshifts, and hence, any purely optically derived model of galaxy formation is likely to be incomplete. *Spitzer* surveys have shown that the cosmic infrared background is dominated by luminous infrared galaxies at around $z \sim 1$ (Dole et al. 2006), while Chapman et al. (2003a) suggest that a large population of highly obscured but very active galaxies at $z = 1-5$ may be the dominant location of massive star formation and AGN fueling at high redshifts. Moreover, there is evidence that these galaxies are strongly clustered, and also have a correlation length exceeding any other known high-$z$ population (Blain et al. 2004; Stevens et al. 2003). These results suggest that these dusty, high-redshift galaxies trace the growth of large-scale structure in the early universe and are the precursors of the massive galaxies in the local universe.

The specific science goals of ATLAS are as follows:

1. To test whether the radio-FIR correlation changes with redshift or with other galaxy properties. Once calibrated, this correlation, which is thought to be driven by active star formation, will be a powerful tool for determining the star formation history of the universe.
2. To search for overdensities of high-$z$ ULIRGs, which mark the positions of protoclusters in the early universe. With a sampling volume of $2 \times 10^7$ Mpc$^3$ deg$^{-2}$ (in the range $z = 1-3$), this survey will contain at least one protocluster with a present-day mass equivalent to Coma. There are expected to be tens of lower mass systems undergoing the first phase of their collapse in this volume, all of which can be detected from the tracer population of the obscured ULIRGs that are thought to reside in such regions (Stevens et al. 2003).
3. To trace the radio luminosity function to a high ($z \sim 1$) redshift for moderate-power sources and measure for the first time the differential 20 cm source count to a flux density limit of $\sim$30 $\mu$Jy to a high precision.
4. To open a region of parameter space, corresponding to a large area of sky surveyed with high sensitivity at radio, mid-IR, and FIR wavelengths, which would enable us to discover rare but important objects, such as short-lived phases in galaxy evolution.

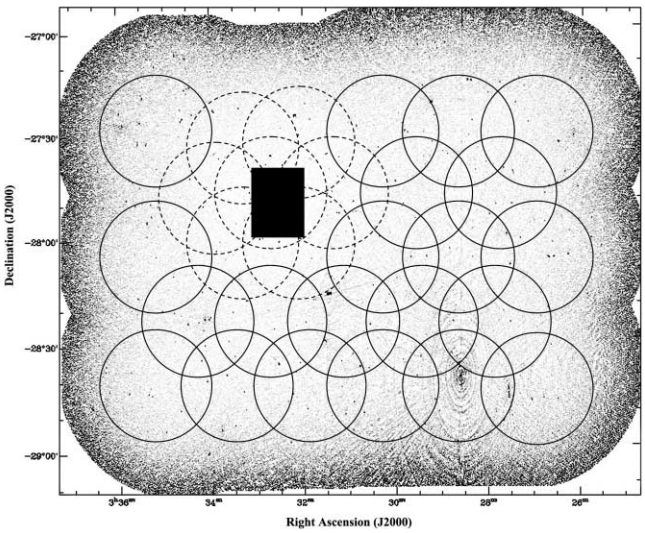


FIG. 1.—Observed fields superposed on the 20 cm image. Circles show the half-power beam width of the ATCA antennas, centered on the pointing positions used in the observations. Solid circles show areas observed in C1241, dashed circles show fields observed in C1035, and the black square shows the GOODS field.

We are currently about halfway through the ATLAS observations, having covered 6 deg$^2$ of the CDF-S and ELAIS-S1 fields to an rms sensitivity of about 40 $\mu$Jy. When the survey is complete, we hope to reach a final rms of 10–15 $\mu$Jy (depending on time allocation) over this field, and will then release data products including FITS images and source catalogs. We also plan to observe the field at another radio wavelength to obtain spectral indices, obtain complementary ground-based optical spectroscopy on the radio sources, and conduct very long baseline interferometry observations of a subset of sources.

In this paper we present the results obtained from the data taken in 2004 in the CDF-S/SWIRE field, to provide a first look at the stronger radio sources in this field.

Throughout this paper we define a radio "component" as a region of radio emission identified in the source extraction process. We define a radio "source" as one or more radio components that appear to be physically connected and that probably correspond to one galaxy. Thus, we count a classical triple radio-loud source as being a radio source consisting of three radio components, but count a pair of interacting starburst galaxies as being two sources, each with one radio component.

Throughout this paper we use the following cosmological parameters: $H_0 = 71$ km s$^{-1}$ Mpc$^{-1}$, $\Omega_m = 0.27$, and $\Omega_\Lambda = 0.73$.

## 2. OBSERVATIONS AND DATA REDUCTION

### 2.1. *Radio Observations and Data Reduction*

The first radio observations of the region surrounding the GOODS field in the CDF-S (AT project C1035) were taken by Koekemoer et al. (2003) and A. Koekemoer et al. (2006, in preparation [hereafter KAMNC]), and have been compared with optical and X-ray data by Afonso et al. (2006). The data were observed over a mosaic of seven overlapping fields, which are shown as dashed lines in Figure 1. A total of 149 hr of integration were used by KAMNC, or 21.3 hr per pointing.

The ATLAS observations (AT project C1241) cover a much wider area, chosen to cover both the CDF-S and ELAIS-S1 SWIRE fields. Here we concentrate solely on the SWIRE/CDF-S region, and all figures here and throughout this paper refer solely to these CDF-S observations. The CDF-S area was covered by a mosaic

TABLE 1
Summary of Radio Observations

| Date | Project ID | Configuration | Time on Source (hr) |
|---|---|---|---|
| 2002 Apr 4–27 | C1035 | 6A | 99 |
| 2002 Aug 24–29 | C1035 | 6C | 50 |
| 2004 Jan 7–12 | C1241 | 6A | 26 |
| 2004 Feb 1–5 | C1241 | 6B | 27 |
| 2004 Jun 6–12 | C1241 | 750D | 63 |
| 2004 Nov 24–30 | C1241 | 6D | 57 |
| Total | | | 322 |

of 21 pointing centers shown in Figure 1. The first observations took place in 2004 January and are expected to continue until 2007. The data used in this paper are those taken up to the end of 2004, and include a total of 173 hr of integration, or 8.2 hr per pointing.

The observations were taken in the AT mosaic mode, in which the array was cycled around the 21 pointing centers, spending about 2 minutes on each, together with observations of the secondary calibrator 0237−233 at least once per cycle. Observations were taken in a variety of array configurations to maximize *u-v* coverage (i.e., the sampling of the Fourier plane). The shortest baseline was 31 m, and the longest was 6000 m. The observing dates and configurations used in this paper are shown in Table 1.

In this paper we use data from both C1035 and C1241. Because noise and sidelobes from our shorter observations extend into the area observed by KAMNC, we do not achieve as high a sensitivity in this region as they did, and we have not taken any special steps to do so. Instead, this paper should be regarded as complementary to the results of KAMNC, who observe a small area with high sensitivity, whereas in this paper we observe a large area with lower sensitivity.

To avoid the regions at the edge of the field, which have significant primary beam attenuation, we restrict the area covered in this paper to the right ascension range $03^{h}26^{m}$ to $03^{h}36^{m}$, and the declination range $-29^{\circ}00'$ to $-27^{\circ}12'$, giving a total surveyed area of about 3.7 deg$^2$.

The CDF-S/ATLAS field contains an unusually strong source (S145 = ATCDFS J032836.53−284156.0) in pointing center 1, which presents a challenge to our calibration procedures, as it is present in the sidelobes of several other pointings. Calibration errors from this source significantly increase the rms noise of the images in this region of the ATLAS field. We have found that a significant contributor to these calibration errors is the noncircularity of the primary beam response of the antennas. While the primary beam response can be measured accurately, current radio-astronomy imaging packages do not enable the data to be corrected for this. Work is in progress both to characterize the primary beam response (using holographic antenna measurements) and to write new calibration software that can apply this information.

All observations were made with two 128 MHz bands, centered on 1344 and 1472 MHz. The correlator was used in continuum mode ($2 \times 128$ MHz bandwidth), with each 128 MHz band divided into $32 \times 4$ MHz channels, and all four Stokes parameters were measured.

The primary flux density calibrator used was PKS B1934−638, which is the standard calibrator for Australia Telescope Compact Array (ATCA) observations ($S = 14.95$ Jy at 1.380 GHz; Reynolds 1994). We calibrated the complex antenna gains by frequently (typically every 20–40 minutes, depending on atmospheric phase stability) observing the secondary calibrator PKS 0237−233. The resulting phase errors are typically at the level of a few degrees before self-calibration and are not a significant limiting factor in the resulting images.

We used the Australia Telescope National Facility release of the MIRIAD (Sault et al. 1995) software to reduce our data. Before imaging, the data from each observing session were inspected, and the MIRIAD interactive tasks *tvflag* and *blflag* were used to flag bad data resulting from interference or hardware problems. The primary calibrator data were flagged before calibration was applied. The secondary calibrator and target data had bandpass and polarization calibration applied before inspection and flagging.

The radio-frequency interference environment at Narrabri deteriorated significantly during the course of the observations: at the start of the observations described here, only minimal flagging was required, whereas by late 2004 about 30% of the data in the second IF had to be deleted because of interference. The data were first flagged using an automated system based on cross-polarization products and were then manually flagged by inspecting rms, amplitude, and phase on each baseline as a function of time.

When imaging, we explored a range of weighting schemes, and eventually chose a superuniform weighting scheme that yielded high spatial resolution, but at the expense of sensitivity. Thus, the rms noise of the images used here is about 50% higher than could be obtained by using natural weighting. For example, KAMNC used robust weighting, with a robustness parameter of 0.5, and thus reached a significantly lower flux density, but at poorer spatial resolution.

Because of the large observing bandwidth ($2 \times 128$ MHz), the multifrequency synthesis (Sault & Wieringa 1994) technique was necessary to improve *u-v* coverage and reduce bandwidth smearing. This technique makes a single image from multifrequency data by gridding each spectral channel in its correct place in the *u-v* plane, instead of at a location determined by the average over all channels.

Bandpasses for each day were calibrated on 1934−638 using *mfcal*, and the resulting bandpass tables copied to other observations on the same day. The first stage of the processing was to image field 1, which contains the strong 1 Jy source ATCDFS J032836.53−284156.0, and then perform four iterations of self-calibration on this source (two with phase only, and the last two with both phase and amplitude). The gain solutions from this self-calibration process were then copied to observations of other fields on the same day. Further self-calibration on other fields was also tried but was not found to improve calibration significantly.

The "individual" approach to mosaicking was taken, in which each pointing field was imaged (using a multifrequency synthesis) and cleaned separately, and then a linear mosaic (using *linmos*) used to mosaic the 28 separate images together. The resulting image has an rms that generally lies in the range 20–60 $\mu$Jy across the field, with a spatial resolution of about $11'' \times 5''$. A representative region of the image is shown in the left panel of Figure 2.

To illustrate the advantage of superuniform weighting, we also show in Figure 2 the same image made with natural weighting. The naturally weighted image has a higher sensitivity but a poorer resolution, resulting in a significantly enhanced confusion rate when cross-identifying with the *Spitzer* observations.

### 2.2. *Component Extraction*

Most source extraction techniques, and all references to a "5 $\sigma$" detection, implicitly assume a Gaussian noise distribution,

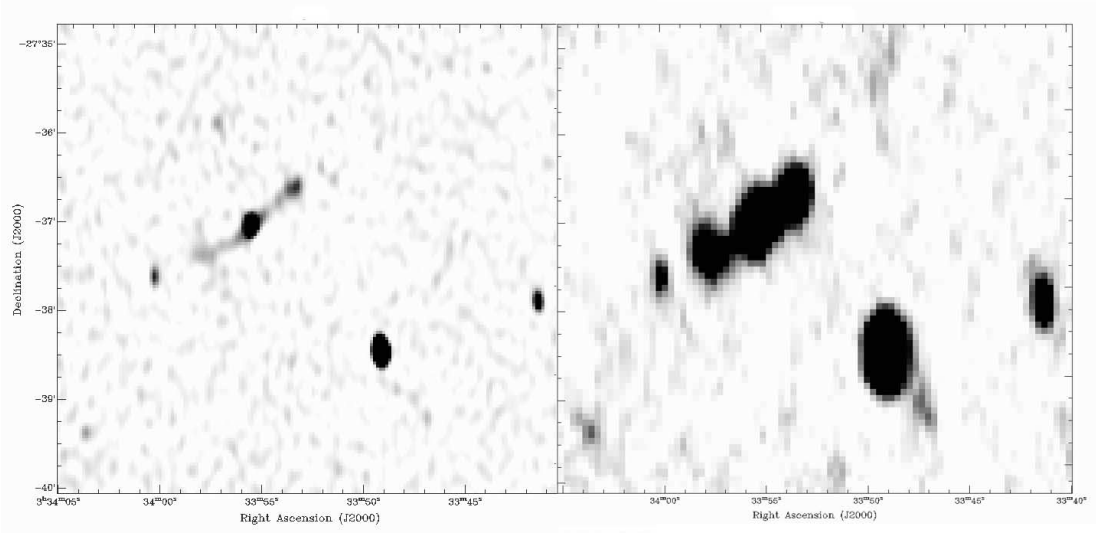


FIG. 2.—*Left*: Representative sample of the radio image used for component identification in this paper, showing a classical triple radio galaxy (C616, C619, and C622) together with other single-component galaxies. This image has a beam size of $11'' \times 5''$ and a local rms noise of 25 $\mu$Jy. *Right*: Same image, but made with natural weighting. It has a higher sensitivity (17 $\mu$Jy rms) but a larger beam size ($28'' \times 16''$).

which is unlikely to be found in radio interferometry images. Nevertheless, an assumption of Gaussian noise can simplify the initial stages of source extraction, and Bondi et al. (2003) have shown SExtractor2 (Bertin & Arnouts 1996) to generate a reliable noise image from radio data. We therefore used SExtractor2 to produce a noise image, which we then divided into the mosaicked image to obtain a signal-to-noise ratio image. The MIRIAD task *imsad* was then used to derive a preliminary list of component "islands" above a cutoff of 4 times the local rms noise. Each component island found by *imsad* was examined and refitted in the mosaicked image data with an elliptical Gaussian to derive component flux densities and sizes. All component images and fit parameters were inspected to check for obvious failures and poor fits that needed further analysis.

In some cases the automated process fitted a single Gaussian profile to a complex of two or more individual components, and so we refitted the data using several Gaussian components. In these cases, each component is listed as a separate component in subsequent analysis.

We then inspected the image of each resulting component. All components with either a peak flux or an integrated flux of less than 5 times the rms noise (as measured by SExtractor2) were discarded unless their morphology strongly suggested their reality, such as the extended source associated with the spiral galaxy S226 (see § 3.6). Some parts of the ATLAS field contain artifacts that result in strongly non-Gaussian noise statistics, so that our simple noise cutoff fails to remove artifacts. Therefore, a subjective approach was used to remove any components that may have been generated or strongly affected by artifacts. The resulting sample therefore does not have a clearly defined sensitivity limit and cannot be used as a statistically complete sample.

In the region of the field where this catalog overlaps with that of KAMNC there is, as expected, overall agreement, but also some significant differences. This is because of the superuniform weighting scheme used here, as compared with the robust weighting scheme used by KAMNC, so the results presented here have lower sensitivity but higher resolution (and also, of course, a lower peak flux for extended sources). Other differences are attributable to different selection procedures. For example, ATCDFS J033159.86−274541.3 appears in the KAMNC catalog but not ours, because it lies on a grating ring (part of the pattern caused by calibration errors) of a nearby strong source and so was rejected by the artifact-removal procedure described above. Close inspection of the KAMNC data shows this component to be real, but it is still excluded from our catalog to maintain consistency.

Comparing the KAMNC fluxes with those presented here reveals the hazards of measuring fluxes in radio-astronomical images with different weighting and gridding schemes. While there is overall agreement, individual sources can differ significantly. For example, ATCDFS J033219.82−274121.2 appears in the KAMNC catalog with a flux density of 0.228 mJy but was missed by our source extraction procedure. Examination of the image used for our source extraction shows this source to be visible but with an integrated flux density of only 0.09 mJy, and so it was rejected by our source selection criterion, whereas it fell above the threshold in the more sensitive KAMNC observations. The difference between the two measured fluxes is consistent with the measured noise levels of the two images at this point (KAMNC place an error estimate of 0.085 mJy on this source).

Comparison of flux densities of all sources common to the two papers shows that our derived integrated flux densities tend to be 14% lower than KAMNC's. This may be partly attributable to the different weighting scheme, but there may also be a small overall calibration difference between the two sets of results. Twenty-seven of our sources also appear in the NRAO VLA Sky Survey (NVSS; Condon et al. 1998). The flux densities we measure are, on average, 11% lower than those listed in NVSS. However, the two surveys have very different synthesized beam sizes (NVSS has $45''$ compared to $6''$ for ATLAS), and so a simple comparison is unreliable.

These differences are, however, higher than expected. Some initial experiments to explore the source of this uncertainty have shown variations of about 10% in flux density depending on imaging parameters such as pixel size and weighting. We plan a set of extensive simulations to explore and understand these differences before the final data release of ATLAS. In the meantime we assign a conservative estimated uncertainty of 20% to all flux densities, in quadrature with the rms noise of the image, which is typically 40 $\mu$Jy. Formal flux density uncertainties from the fitting process are generally low compared to this uncertainty

TABLE 2
SWIRE Resolution and Sensitivity

| Band | Limiting (5 $\sigma$) Sensitivity ($\mu$Jy) | FWHM Resolution (arcsec) |
|---|---|---|
| 3.6 $\mu$m | 5 | 1.2 |
| 4.5 $\mu$m | 9 | 1.2 |
| 5.8 $\mu$m | 43 | 1.2 |
| 8 $\mu$m | 40 | 2.0 |
| 24 $\mu$m | 192.5 | 5.5 |

due to calibration, and so are not listed individually. We expect to derive more rigorous flux density uncertainty estimates in the final ATLAS catalog.

### 2.3. *Spitzer Observations*

*Spitzer* was launched in 2003 August. It is equipped with several instruments, and here we use data taken with the Infrared Array Camera (IRAC) at each of four bands (3.6, 4.5, 5.8, and 8 $\mu$m) and with the Multiband Imaging Photometer for *Spitzer* (MIPS) in its 24 $\mu$m band.

Before launch, proposals were invited for Legacy Science Programs, large coherent programs whose data would be of lasting importance to the broad astronomical community. One of the six Legacy projects chosen was the SWIRE Survey (Lonsdale et al. 2003), which has observed a 6 deg$^2$ region surrounding the CDF-S. The analysis of those data is described by J. Surace et al. (2006, in preparation) and has resulted in images to depths of 5, 9, 43, 40, and 193 $\mu$Jy, respectively, in the four IRAC bands and in the 24 $\mu$m MIPS band, together with a catalog of detected sources. Most of the SWIRE data are now in the public domain.[10] Here we use the SWIRE Public Data Release 3.

The IRAC and MIPS fluxes used here are, in the case of unresolved or noisy sources, aperture-corrected fluxes, as described by J. Surace et al. (2006, in preparation). In the case of extended sources, Kron fluxes are used (Kron 1980).

In some cases we give infrared fluxes and SWIRE identifications for sources that do not appear in the public-release SWIRE catalog, because the public catalog sensitivity is set at a more conservative threshold level than that used here. However, all SWIRE sources listed here are visible in the SWIRE images that are also in the public domain. Table 2 shows the approximate resolution and sensitivity at each wavelength resulting from the SWIRE Survey.

[10] See http://swire.ipac.caltech.edu/swire/astronomers/data_access.html.

### 2.4. *Optical Photometry*

In support of the SWIRE Legacy program, the CDF-S field was observed for 18 nights with the MOSAIC II camera on the Blanco 4 m Telescope at Cerro Tololo. Fifteen pointings covered 4.5 deg$^2$ in four filters ($U$ or $u'$, $g'$, $r'$, and $i'$) to 5 $\sigma$ depths of $\sim$24.5, 25.4, 25, and 24 Vega magnitudes, respectively, with an additional 1.5 deg$^2$ in $z'$ to 23.3. Filter characteristics are given in Table 3. In addition, there is one deep pointing (25.2, 25.7, 25.5, and 24.5) covering 0.33 deg$^2$ centered at $03^h31^m14^s$, $-28^\circ36'$. The optical data overlap $\sim$2.6 deg$^2$ of the primary radio data. Seeing ranged from 0.″9 to 1.″6 in mostly photometric weather. The pointings that were observed in photometric conditions were calibrated using photometric standards observed throughout the night. The nonphotometric pointings were calibrated by cross-correlating sources that overlap regions of photometric fields. The calibration uncertainty is estimated to be 3% in $g'$, $r'$, and $i'$ and 5% in $U$ and $z'$.

### 2.5. *Spectroscopy*

We obtained spectra of a subset of the radio sample in two separate observing sessions. The first was part of the Australian Deep Radio Optical Infrared Target (ADROIT) survey, which used the Two Degree Field (2dF) multifiber spectrometer on the Anglo-Australian telescope (AAT) in the period of 2003 November 19–25. The 316R (spectrograph 1) and 270R (spectrograph 2) gratings were used giving dispersions of 4.09 and 4.77 Å pixel$^{-1}$, respectively. We split our targets into two samples, bright ($R < 21$) and faint ($21 < R < 23$).

The bright sample was observed in the normal 2dF observing mode with both spectrographs, while the faint sample was observed in nod-and-shuffle mode (Glazebrook & Bland-Hawthorn 2001). The bright field contained 64 targets going to spectrograph 1 and 65 going to spectrograph 2.

The faint configuration had 43 targets, all of which went to spectrograph 1. The field was configured such that each object was allocated two fibers. Each pair of fibers was positioned at an A and B position, where A was the true position of the source and B was offset by 60″ in right ascension. Two of the four guide fibers were allocated to each of the A and B positions. A flat and arc were taken without the mask on, and then the mask was positioned and the telescope slewed to the field. A second flat and arc were taken with the mask in place, and this was repeated every few hours between science observations. Each target exposure consisted of 60 s at position A followed by 60 s at position B, repeated 15 times before the detector was read out. Each time the telescope was nodded between A and B, the charge would be shuffled back and forth in the detector by 50 pixels (in the $Y$-direction). Each exposure therefore consisted of 900 s at

TABLE 3
Filter Characteristics Used for Optical Photometry

| Filter | NOAO Name | Effective Wavelength (nm) | Limiting Magnitude | Vega to AB Conversion |
|---|---|---|---|---|
| $u'$ | | 361.8 | 24.5 | 0.90 |
| $U$ | c6001 | 366.7 | 24.5 | 0.73 |
| $g'$ | c6017 | 476.4 | 25.4 | −0.10 |
| $r'$ | c6018 | 627.9 | 25 | 0.16 |
| $i'$ | c6019 | 764.7 | 24 | 0.39 |
| $z'$ | c6020 | 869.0 | 23.3 | 0.55 |

Notes.—All magnitudes given in this paper are in the Vega system. They can be converted to AB magnitudes by adding the number in the last column. The limiting magnitudes are the 5 $\sigma$ limits obtained over most of the field. Deeper limits were obtained in the region of the GOODS field, as described in § 2.4.

position A and 900 s at position B. In total 19 nod-and-shuffle exposures were taken on the nights of November 19, 22, 23, 24, and 25. Some nights were affected by cloud, and the seeing was variable, with a median of 2.″1 (full range of 1.″3–3.″0). Therefore, we obtained a total of 48,600 s (13.5 hr) exposure for each source ($2 \times 27 \times 900$ s).

The data from the bright configuration were reduced using the standard 2dFDR routines. The resulting mean signal-to-noise ratios were 16.4 (spectrograph 1) and 16.8 (spectrograph 2). The combined data were then run through a final program NS_comb-AB, which combined the A and B observations of each target. The mean signal-to-noise ratio in the final combined frames was 2.34 (2dFDR flux weighting) or 2.26 (2dFDR unweighted), from an effective exposure time of 34,200 s or 9.5 hr. The spectra were analyzed using the 2004 April version of the RUNZ code used for the 2dF Galaxy Redshift Survey and 2dF–Sloan Digital Sky Survey (SDSS) Luminous Red Galaxy surveys.

The second set of spectroscopic observations was obtained using the AAOmega, the new spectrograph back end to the AAT's 2dF multifiber spectrometer. AAOmega is a dual-arm bench-mounted spectrograph and provides greater throughput, stability, and resolution than the previous 2dF spectrographs. Our observations were made on 2006 January 26–28 as part of the AAOmega Science Verification program.

We used the 580V and 385R volume-phase holographic gratings in the blue and red arms, respectively, providing a resolution of 1300 and dispersions of 0.1 nm pixel$^{-1}$ (blue) and 0.16 nm pixel$^{-1}$ (red). In both arms there are $\sim$3.5 pixels per resolution element. Our observations were the first to make use of the nod-and-shuffle mode built into AAOmega. As above we allocated two fibers to each field, using a new version of the 2dF *configure* software, applying a simulated annealing algorithm to maximize the number of fiber pairs configured (Miszalski et al. 2006). A total of 78 objects were configured. The A and B positions for the targets were separated by 120″, and observations were carried out as described above, with each exposure consisting of 60 s at position A followed by 60 s at position B, repeated 15 times. Thus, each data frame has an effective exposure time of 1800 s on target. Over the three nights we obtained $12 \times 1800$ s on target in seeing of 1.″2–1.″5, so a total of 6 hr of on-source integration was acquired. The median signal-to-noise ratios for objects in the $R$ magnitude ranges 20.0–20.5, 20.5–21.0, 21.0–21.5, 21.5–22.0, and 22.0–22.5 are 10.6, 6.5, 3.1, 3.2, and 1.7, respectively. Redshifts were measured using the 2006 May version of the RUNZ code, and their reliability was assessed manually. Twenty-three of the 25 objects at $R < 21$ produced reliable redshifts, and 30 of the 47 targets at $21 < R < 23$ produced reliable redshifts. One of the six objects fainter than $R = 23$ had a reliable redshift.

## 3. RESULTS AND ANALYSIS

### 3.1. *The Image Data*

Representative portions of the 20 cm image of the CDF-S/SWIRE field are given in Figures 2 and 3. Postage stamp images of all sources will be available from the NASA/IPAC Extragalactic Database.[11]

### 3.2. *The Component Catalog*

Radio components were extracted from the image as described in § 2.2. Table 4 shows the resulting catalog, which contains 784 radio components. The fields of Table 4 are as follows:

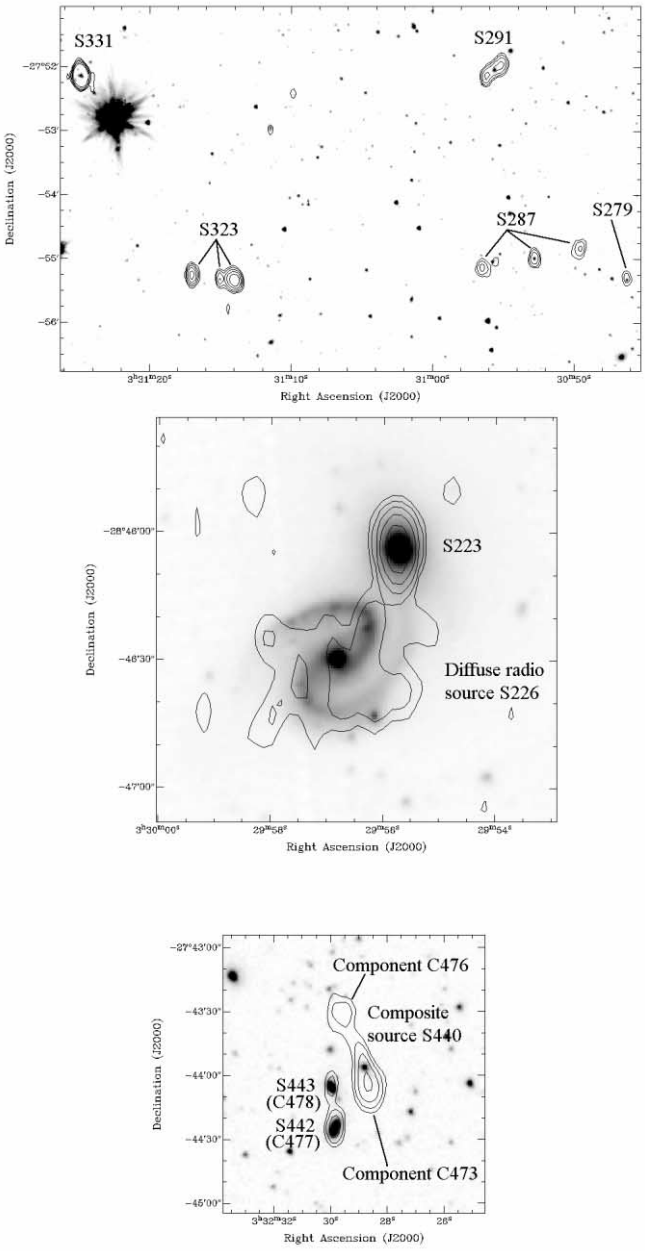


FIG. 3.—Representative 20 cm images of three regions containing radio sources (*contours*) overlaid on the 3.6 $\mu$m *Spitzer* images (*gray scale*).

*Column* (*1*).—Component number. This is the internal designation of the component used within this paper.

*Column* (*2*).—Designation for this radio component. In the case of single-component sources, this is identical to the source name used in Table 6.

*Column* (*3*).—Right ascension (J2000.0).

*Column* (*4*).—Declination (J2000.0).

*Columns* (*5*) *and* (*6*).—The rms uncertainties in right ascension and declination. These include the formal uncertainties derived from the Gaussian fit together with a potential systematic error in the position of the calibrator source of 0.″1. Comparison of our positions with *Spitzer* positions in § 3.3 below shows that these estimated uncertainties are realistic.

*Column* (*7*).—Peak flux density at 20 cm (in millijanskys) of the fitted Gaussian component. The estimated uncertainty is 20% in quadrature, with the rms given in column (12).

[11] See http://nedwww.ipac.caltech.edu.

TABLE 4

CATALOG OF RADIO COMPONENTS

| ID No. (1) | Name (2) | Radio R.A. (3) | Radio Decl. (4) | Err(R.A.) (arcsec) (5) | Err(Decl.) (arcsec) (6) | Peak Flux (mJy) (7) | Int. Flux (mJy) (8) | Beam Major Axis (arcsec) (9) | Beam Minor Axis (arcsec) (10) | Beam P.A. (deg) (11) | rms (uJy beam$^{-1}$) (12) | Comment (13) |
|---|---|---|---|---|---|---|---|---|---|---|---|---|
| C001..... | ATCDFS J032602.78−284709.0 | 3 26 02.785 | −28 47 09.06 | 0.78 | 0.73 | 0.70 | 1.38 | 8.3 | 2.6 | 60.8 | 79.3 | |
| C002..... | ATCDFS J032604.15−275659.3 | 3 26 04.152 | −27 56 59.39 | 0.55 | 0.90 | 0.71 | 1.97 | 11.5 | 7.3 | −17.0 | 71.9 | |
| C003..... | ATCDFS J032605.68−274734.4 | 3 26 05.685 | −27 47 34.48 | 0.10 | 0.11 | 40.81 | 74.70 | 5.9 | 5.6 | 85.7 | 119.1 | |
| C004..... | ATCDFS J032606.95−275332.2 | 3 26 06.955 | −27 53 32.26 | 0.52 | 1.19 | 0.41 | 0.43 | 0.0 | 0.0 | −1.0 | 76.7 | |
| C005..... | ATCDFS J032611.47−273243.8 | 3 26 11.475 | −27 32 43.81 | 0.10 | 0.10 | 69.65 | 110.90 | 5.3 | 3.3 | 89.6 | 156.3 | |
| C006..... | ATCDFS J032613.70−281717.7 | 3 26 13.701 | −28 17 17.71 | 0.57 | 0.79 | 0.48 | 0.54 | 0.0 | 0.0 | 0.0 | 77.7 | |
| C007..... | ATCDFS J032615.48−284629.2 | 3 26 15.489 | −28 46 29.24 | 0.34 | 0.36 | 0.45 | 0.71 | 0.0 | 0.0 | 0.0 | 66.0 | |
| C008..... | ATCDFS J032615.55−280601.0 | 3 26 15.557 | −28 06 01.05 | 0.30 | 0.47 | 0.73 | 1.06 | 0.0 | 0.0 | −1.0 | 56.9 | |
| C009..... | ATCDFS J032616.35−280014.6 | 3 26 16.353 | −28 00 14.61 | 0.18 | 0.30 | 1.24 | 1.66 | 0.0 | 0.0 | −1.0 | 60.1 | |
| C010..... | ATCDFS J032616.41−271621.1 | 3 26 16.419 | −27 16 21.10 | 0.15 | 0.23 | 4.17 | 7.84 | 9.1 | 2.8 | −40.0 | 90.2 | |
| C011..... | ATCDFS J032617.43−280709.9 | 3 26 17.430 | −28 07 09.95 | 0.19 | 0.24 | 6.73 | 13.83 | 8.6 | 3.3 | 58.2 | 57.6 | South lobe of radio double |
| C012..... | ATCDFS J032618.22−280703.5 | 3 26 18.225 | −28 07 03.54 | 0.47 | 0.46 | 3.80 | 10.29 | 11.2 | 3.9 | 70.0 | 57.4 | North lobe of radio double |
| C013..... | ATCDFS J032622.07−274324.4 | 3 26 22.079 | −27 43 24.48 | 0.10 | 0.12 | 17.35 | 27.81 | 5.5 | 4.4 | 35.4 | 71.7 | |
| C014..... | ATCDFS J032625.10−280908.8 | 3 26 25.109 | −28 09 08.85 | 0.63 | 0.85 | 0.41 | 0.96 | 9.0 | 5.0 | 62.1 | 57.1 | |
| C015..... | ATCDFS J032626.90−275610.9 | 3 26 26.904 | −27 56 10.91 | 0.14 | 0.21 | 2.65 | 4.14 | 6.6 | 3.6 | −26.1 | 62.6 | |

NOTES.—Units of right ascension are hours, minutes, and seconds, and units of declination are degrees, arcminutes, and arcseconds (J2000.0). Table 4 is published in its entirety in the electronic edition of the *Astronomical Journal*. A portion is shown here for guidance regarding its form and content.

TABLE 5
Cross-Identifications and Expected False Cross-Identification Rate

| ID Type | Description | No. Components | No. Sources | No. Spurious |
|---|---|---|---|---|
| 1 | Within 1″ of SWIRE source | 393 | 393 | 15.3 |
| 2 | 1″–2″ from SWIRE source | 167 | 167 | 19.2 |
| 3 | 2″–3″ from SWIRE source | 57 | 57 | 21.2 |
| 4 | Good ID but >3″ | 31 | 31 | 0 |
| −1 or 5 | Part of a classical radio double | 46 | 23 | 0 |
| 6 | Part of a classical radio triple | 33 | 11 | 0 |
| 7 | IRAC source, not in SWIRE catalog | 17 | 17 | 0 |
| 8 | Outside SWIRE region | 5 | 5 | 0 |
| 9 | IFRS | 22 | 22 | 0 |
| 10 | Part of another source (e.g., knots in jets) | 13 | 0 | 0 |

*Column* (*8*).—Integrated flux density at 20 cm (in millijanskys) of the fitted Gaussian component. The estimated uncertainty is 20% in quadrature, with the rms given in column (12).

*Columns* (*9*) *and* (*10*).—Deconvolved FWHM major and minor axes (in arcseconds) of the Gaussian fit. If the undeconvolved fitted major or minor axis size was within one formal standard error of the restoring beam size, it was set to zero.

*Column* (*11*).—Major-axis position angle (in degrees east of north).

*Column* (*12*).—The value (in microjanskys per beam) of the rms map generated by SExtractor at the position of the component.

*Column* (*13*).—Comment.

### 3.3. *Radio-Infrared Cross-Identifications and Identification of Multicomponent Sources*

Although the spatial resolution of the radio image is typically $\theta_{\rm HPBW} \sim 6''$, the positional error for an unresolved source in the presence of Gaussian noise is expected to be on the order of $\theta_{\rm HPBW}$/SNR (Condon 1997), where SNR is the signal-to-noise ratio, and should therefore be on the order of 1″ or less for the unresolved radio components discussed in this paper. This expectation is largely confirmed by the source statistics discussed below. The SWIRE positional errors were in all cases less than 1″.

We note that other authors (e.g., de Ruiter et al. 1977) have used automated techniques for performing cross-identifications and estimating the error rate, but we do not consider these techniques to be appropriate here because of the presence of sidelobes, extended sources, and multiple components, which make automated techniques less reliable. In most of the cases discussed here, the identification is unambiguous because of the relatively low density (compared to the source size and positional accuracy) of sources in both the radio and SWIRE images, and we estimate the error rate by repeating the identification process using spatially shifted data.

For the cross-identifications we used a prerelease version of the SWIRE Public Data Release 3 catalog. The version that was publicly released is slightly more conservative than this prerelease version, and so some identifications do not appear in the public data release. However, all are visible on the publicly released SWIRE images.

For each radio component we initially searched the SWIRE catalog for a source at any *Spitzer* wavelength within 3″, and counted the nearest such source as a correct identification, unless subsequently reclassified on the basis of morphology (see below). This resulted in a distribution of distance to the nearest identification shown in Table 5. About half the radio components have a SWIRE source within 1″, and 79% have a SWIRE source within 3″. For the 163 radio components that did not have an identification within 3″, we examined each source in turn, using both the radio and infrared images.

In 46 cases, the radio components formed a classical double radio source, in which the host galaxy lies roughly midway between the two radio lobes. A further 33 components were members of classical radio triple sources, in which a SWIRE source was coincident with the center radio component, and no SWIRE source was visible coincident with the lobes. In 31 cases, the radio component appeared to be associated with a SWIRE source even though their central positions differed by more than 3″, typically because the source was extended. In 17 cases, a source was visible on the *Spitzer* images but had not been included in the SWIRE catalog either because it was too faint or because it was confused by a nearby bright source, and in five cases the radio source lay in a region that was outside the area observed in the SWIRE project. These statistics are summarized in Table 5.

As a further check on multiple sources, quite independent of the above process, we applied the technique described by Magliocchetti et al. (1998), in which a pair of radio components are classified as the lobes of a double radio source if they satisfy the criteria (1) $\theta < 100(S/100)^{1/2}$, where $S$ is their combined total flux in millijanskys and $\theta$ is their separation in arcseconds, and (2) $0.25 < S_1/S_2 < 4$, where $S_1$ and $S_2$ are the integrated flux densities of the two components. This technique has the advantages of being objective and of having been demonstrated to work well at millijansky flux densities. It has the disadvantages that it is untested at the flux densities observed here (where interacting starburst galaxies, for example, are far more common than at higher flux density levels) and that it does not make use of the additional information available from the *Spitzer* data. This is discussed further in § 3.6 below.

Nevertheless, the two techniques show remarkable agreement. The Magliocchetti et al. (1998) test (hereafter called the *M*-test) missed only five of the 34 sources classified as triples or doubles by the subjective technique and found a further two doubles that had been missed by the subjective technique. In addition, it identified 13 groups of sources that had been recognized as potential double or multiple sources in the subjective technique but that had subsequently been classified as neighbors, clusters, or interacting galaxies on the basis of their morphology or *Spitzer* identifications. For example, the pair of components C072 and C073 survives the *M*-test, but both have subarcsecond *Spitzer* identifications. The probability of two sources both having spurious subarcsecond *Spitzer* identifications is $4 \times 10^{-4}$, and so we classify these as two separate galaxies. All cases in which the two techniques disagreed were reexamined, and the verdict noted in the comments column of Table 6.

TABLE 6
CATALOG OF RADIO SOURCES WITH THEIR IDENTIFICATIONS AND CLASSIFICATIONS

| ID No. (1) | Name (2) | Component No. (3) | SWIRE ID (4) | Radio R.A. (5) | Radio Decl. (6) | 20 cm Flux ($\mu$Jy) (7) | 3.6 $\mu$m Flux ($\mu$Jy) (8) |
|---|---|---|---|---|---|---|---|
| S130 ..... | ATCDFS J032822.70−283157.7 | C140 | SWIRE3 J032822.69−283157.9 | 3 28 22.701 | −28 31 57.77 | 1.3 | 3948.5 |
| S131 ..... | ATCDFS J032823.93−281519.8 | C142 | SWIRE3 J032823.95−281520.0 | 3 28 23.931 | −28 15 19.84 | 0.6 | 822.8 |
| S132 ..... | ATCDFS J032824.45−281837.5 | C143 | SWIRE3 J032824.52−281839.8 | 3 28 24.454 | −28 18 37.59 | 0.2 | 165.9 |
| S133 ..... | ATCDFS J032824.56−284021.7 | C144 | SWIRE3 J032824.56−284021.6 | 3 28 24.567 | −28 40 21.79 | 11.1 | 14.7 |
| S134 ..... | ATCDFS J032824.71−274149.8 | C145, C147 | SWIRE3 J032824.71−274149.3 | 3 28 24.712 | −27 41 49.85 | 1.4 | 46.4 |
| S135 ..... | ATCDFS J032825.37−274445.5 | C146 | SWIRE3 J032825.35−274445.0 | 3 28 25.373 | −27 44 45.50 | 1.0 | 30.4 |
| S136 ..... | ATCDFS J032825.92−271701.3 | C141, C148, C151 | SWIRE3 J032825.92−271701.3 | 3 28 25.92 | −27 17 01.32 | 34.2 | 38.1 |
| S137 ..... | ATCDFS J032826.50−281920.5 | C149 | SWIRE3 J032826.51−281920.7 | 3 28 26.504 | −28 19 20.57 | 1.2 | 589.1 |
| S138 ..... | ATCDFS J032826.55−273304.2 | C150 | SWIRE3 J032826.52−273304.1 | 3 28 26.556 | −27 33 04.25 | 4.1 | 105.0 |
| S139 ..... | ATCDFS J032829.30−280151.0 | C152 | SWIRE3 J032829.30−280150.5 | 3 28 29.309 | −28 01 51.01 | 1.6 | 294.4 |
| S140 ..... | ATCDFS J032832.77−273538.7 | C153 | SWIRE3 J032832.78−273540.2 | 3 28 32.773 | −27 35 38.76 | 0.6 | 238.1 |
| S141 ..... | ATCDFS J032832.79−285536.3 | C154 | SWIRE3 J032832.78−285536.1 | 3 28 32.797 | −28 55 36.34 | 17.3 | 42.9 |
| S142 ..... | ATCDFS J032833.79−280152.5 | C155 | SWIRE3 J032833.78−280153.5 | 3 28 33.798 | −28 01 52.55 | 0.3 | 19.8 |
| S143 ..... | ATCDFS J032835.63−273515.1 | C156 | SWIRE3 J032835.53−273514.2 | 3 28 35.631 | −27 35 15.14 | 3.2 | 36.1 |
| S144 ..... | ATCDFS J032836.22−271650.3 | C157 | SWIRE3 J032836.19−271650.3 | 3 28 36.220 | −27 16 50.38 | 0.8 | 52.2 |
| S145 ..... | ATCDFS J032836.53−284156.0 | C158, C159 | SWIRE3 J032836.52−284156.0 | 3 28 36.53 | −28 41 56.00 | 1357.8 | 4030.0 |
| S146 ..... | ATCDFS J032837.04−275434.9 | C160 | SWIRE3 J032837.04−275435.0 | 3 28 37.049 | −27 54 34.93 | 0.6 | 776.0 |
| S147 ..... | ATCDFS J032840.34−280539.9 | C161 | SWIRE3 J032840.34−280539.2 | 3 28 40.342 | −28 05 39.98 | 0.6 | 17.1 |
| S148 ..... | ATCDFS J032841.10−283644.3 | C162 | SWIRE3 J032841.23−283646.6 | 3 28 41.102 | −28 36 44.36 | 2.2 | 113.2 |
| S149 ..... | ATCDFS J032842.40−274447.7 | C163 | SWIRE3 J032842.41−274446.5 | 3 28 42.401 | −27 44 47.79 | 0.3 | 42.9 |
| S150 ..... | ATCDFS J032843.38−282157.7 | C164 | SWIRE3 J032843.33−282157.2 | 3 28 43.386 | −28 21 57.75 | 1.3 | 203.0 |
| S151 ..... | ATCDFS J032844.28−282323.0 | C165 | SWIRE3 J032844.22−282323.5 | 3 28 44.288 | −28 23 23.04 | 1.0 | 38.2 |
| S152 ..... | ATCDFS J032846.65−282616.6 | C166 | SWIRE3 J032846.56−282618.1 | 3 28 46.651 | −28 26 16.64 | 58.0 | 96.4 |
| S153 ..... | ATCDFS J032847.23−271512.9 | C167 | SWIRE3 J032847.21−271513.1 | 3 28 47.231 | −27 15 12.93 | 6.0 | 12.3 |
| S154 ..... | ATCDFS J032848.75−283523.6 | C168, C169 | SWIRE3 J032848.75−283523.6 | 3 28 48.75 | −28 35 23.68 | 4.2 | 35.2 |
| S155 ..... | ATCDFS J032850.97−273826.8 | C170 | SWIRE3 J032850.93−273827.1 | 3 28 50.977 | −27 38 26.87 | 0.4 | 78.4 |
| S156 ..... | ATCDFS J032851.61−280544.6 | C171 | SWIRE3 J032851.63−280544.3 | 3 28 51.610 | −28 05 44.62 | 4.2 | 29.0 |
| S157 ..... | ATCDFS J032853.28−275401.3 | C172 | SWIRE3 J032853.28−275401.0 | 3 28 53.287 | −27 54 01.35 | 0.3 | 180.7 |
| S158 ..... | ATCDFS J032854.03−273835.7 | C173 | SWIRE3 J032853.99−273835.4 | 3 28 54.031 | −27 38 35.75 | 0.8 | 42.1 |
| S159 ..... | ATCDFS J032854.45−271810.0 | C174 | | 3 28 54.452 | −27 18 10.02 | 0.3 | −1.0 |

NOTES.—Units of right ascension are hours, minutes, and seconds, and units of declination are degrees, arcminutes, and arcseconds (J2000.0). Table 6 is published in its entirety in the electronic edition of the *Astronomical Journal*. A portion is shown here for guidance regarding its form and content.

At the end of this cross-identification process, 22 radio sources remained that did not have SWIRE counterparts. While the weakest of these might be due to noise peaks in the radio image that had falsely been counted as radio sources, there remain eight sources for which there is an unambiguous radio source with an integrated flux of at least 1 mJy, and for which a good SWIRE image at that position shows no indication of an infrared source. We call these sources "infrared-faint radio sources" (IFRSs) and discuss them in more detail in § 4.3 below.

We estimated the probability of false cross-identifications by shifting all the radio sources by 1′ and repeating the process. As a result, we estimated that 15.25 of the 393 cross-identifications within 1″ (i.e., 3.9%) are false, 19.20 of the 167 (11.5%) between 1″ and 2″ are false, and 21.20 of the 57 (37.2%) between 2″ and 3″ are false.

After grouping together multiple radio components that appear to be physically part of one radio source as described above, the 784 radio components correspond to 726 radio sources (including the IFRSs), which are identified with 682 SWIRE sources. We estimate 56 of these (or 8.2%) to be spurious identifications caused by confusion in the IRAC data.

Any systematic error in our positions should show up as a systematic offset between our positions and the *Spitzer* positions. The mean position offset between *Spitzer* and radio positions, averaged over all sources with a *Spitzer* identification, is 0.″06 and 0.″11 in right ascension and declination, respectively. Restricting the comparison to sources for which the *Spitzer* identification is within 3″ of the radio source gives mean offsets of 0.″04 and 0.″09, respectively.

After the cross-identification process was completed, the SWIRE Public Data Release 3 became available, which is slightly more conservative than the version used for the cross-identification and does not include some faint or confused sources. Of the 682 identifications with previously cataloged sources, 82 did not appear in the SWIRE Public Data Release 3. In each of these cases, the SWIRE images were reexamined, and in 74 cases the identification with the previously cataloged source was confirmed. These sources do not have a formal "SWIRE3 J. . ." designation, and instead appear in Table 6 with their internal identification numbers in brackets. In the reappraisal of the remaining eight cases, the identification was changed to the SWIRE source that appears in the public data release.

### 3.4. *Source Characterization*

Sources were characterized using the following criteria. The letters correspond to column (21) in Table 6.

*a*.—If the radio morphology indicates a classical radio double or triple source, or a core-jet source, then it is classified as an AGN. Thirty-five sources were classified in this way.

TABLE 6—*Continued*

| ID No. (1) | 4.5 $\mu$m Flux ($\mu$Jy) (9) | 5.8 $\mu$m Flux ($\mu$Jy) (10) | 8.0 $\mu$m Flux ($\mu$Jy) (11) | 24 $\mu$m Flux ($\mu$Jy) (12) | *U* (13) | *G* (14) | *R* (15) | *I* (16) | *Z* (17) | *z* (Spectral) (18) | ID Type (19) | Class (20) | Basis (21) | Comments (22) |
|---|---|---|---|---|---|---|---|---|---|---|---|---|---|---|
| S130 ..... | 2722.9 | 3570.3 | 21307.8 | 15713.7 | 18.7 | 17.9 | 17.1 | 16.4 | | | 1 | | | |
| S131 ..... | 888.4 | 1225.0 | 4898.1 | 11087.7 | | | | | | 0.1214 | 1 | | | *z*(g) |
| S132 ..... | 232.6 | 340.5 | 489.2 | 2290.4 | | | | | | | 3 | | | |
| S133 ..... | 13.2 | −1.0 | −1.0 | −1.0 | 99.0 | 99.0 | 99.0 | 99.0 | | | 1 | | | |
| S134 ..... | 55.0 | 71.4 | −1.0 | 505.2 | 99.0 | 99.0 | 99.0 | 99.0 | | | 1 | AGN | b | Core-jet |
| S135 ..... | 32.7 | 43.8 | −1.0 | −1.0 | | | | | | | 1 | | | |
| S136 ..... | 25.9 | −1.0 | −1.0 | −1.0 | | | | | | | −1 | AGN | a | Radio double with connecting jet |
| S137 ..... | 483.3 | 146.7 | 133.9 | 580.0 | 99.0 | 21.9 | 20.2 | 99.0 | | 0.4265 | 1 | AGN | b | *z*(b) |
| S138 ..... | 83.2 | 51.6 | 41.2 | −1.0 | 99.0 | 99.0 | 99.0 | 22.7 | | | 1 | | | |
| S139 ..... | 166.4 | 106.5 | 72.1 | −1.0 | 99.0 | 24.5 | 22.3 | 20.8 | | 0.9021 | 1 | | | *z*(b) |
| S140 ..... | 174.7 | 176.2 | 2183.9 | 3603.7 | 20.2 | 19.9 | 19.3 | 18.7 | | | 2 | | | |
| S141 ..... | 49.5 | 49.5 | −1.0 | −1.0 | 99.0 | 24.3 | 23.6 | 22.5 | | | 1 | | | |
| S142 ..... | 18.4 | −1.0 | −1.0 | −1.0 | 99.0 | 99.0 | 99.0 | 99.0 | | | 1 | | | |
| S143 ..... | 36.0 | −1.0 | −1.0 | −1.0 | 99.0 | 99.0 | 99.0 | 99.0 | | | 2 | | | |
| S144 ..... | 54.6 | −1.0 | 37.4 | −1.0 | | | | | | | 1 | | | |
| S145 ..... | 5687.8 | 9769.3 | 24294.5 | 202434.7 | 18.6 | 18.3 | 17.6 | 16.7 | | 0.1084 | −1 | AGN | ab | Radio double. Strongest radio source in field. Failed *M*-test because of flux ratio. *z*(g) |
| S146 ..... | 513.2 | 731.6 | 4758.2 | 6575.6 | 18.6 | 18.5 | 18.0 | 17.5 | | | 1 | | | |
| S147 ..... | 20.7 | −1.0 | −1.0 | 199.2 | 99.0 | 99.0 | 99.0 | 23.6 | | | 1 | AGN | b | |
| S148 ..... | 56.2 | 52.9 | 34.3 | −1.0 | 99.0 | 24.5 | 22.9 | 21.5 | | | 4 | | | |
| S149 ..... | 36.8 | 37.1 | −1.0 | −1.0 | | | | | | | 2 | | | |
| S150 ..... | 154.4 | 98.9 | 48.2 | −1.0 | 99.0 | 22.0 | 20.3 | 19.2 | | 0.4276 | 1 | | | *z*(b) |
| S151 ..... | 52.6 | 66.1 | 86.0 | 409.2 | 99.0 | 99.0 | 99.0 | 99.0 | | | 1 | AGN | b | |
| S152 ..... | 84.5 | 102.2 | 83.9 | −1.0 | 99.0 | 99.0 | 99.0 | 99.0 | | | 2 | | | |
| S153 ..... | 19.1 | −1.0 | −1.0 | −1.0 | | | | | | | 1 | | | |
| S154 ..... | 30.7 | −1.0 | 52.4 | 427.5 | 99.0 | 99.0 | 24.0 | 22.5 | | | −1 | AGN | ab | Radio double |
| S155 ..... | 58.2 | 40.9 | −1.0 | −1.0 | 99.0 | 99.0 | 23.6 | 22.5 | | | 1 | | | |
| S156 ..... | 35.1 | −1.0 | −1.0 | −1.0 | 99.0 | 99.0 | 99.0 | 99.0 | | | 1 | | | |
| S157 ..... | 163.9 | 48.2 | −1.0 | −1.0 | 99.0 | 99.0 | 99.0 | 22.2 | | | 1 | | | |
| S158 ..... | 25.2 | −1.0 | −1.0 | −1.0 | 99.0 | 99.0 | 22.9 | 21.6 | | | 1 | | | |
| S159 ..... | −1.0 | −1.0 | 303.0 | −1.0 | | | | | | | 7 | | | Weak uncataloged source in IRAC band 1 |

*b*.—If the radio source is stronger than the radio-FIR correlation by a factor of 10 [i.e., $\log(S_{24\ \mu m}/S_{20\ cm}) < 0$], then it is classified as an AGN. One-hundred-thirteen sources were classified in this way. We note that all sources classified as AGNs by criterion 1 that had a measured 24 $\mu$m flux would also have been classified as an AGNs by this criterion. Despite potential *K*-corrections to both the radio and infrared fluxes, the slope of the radio-FIR correlation does not appear to vary strongly with redshift (Appleton et al. 2004; Higdon et al. 2005), and so this criterion should be useful at all redshifts.

*c*.—If a source is classified by other authors (either Afonso et al. [2006] or Croom et al. [2001]) on the basis of its spectroscopic or X-ray properties, then we assign it their classification. Eight sources were classified as AGNs in this way, and 5 as star-forming galaxies.

*s*.—Although the spectroscopy was mainly targeted at obtaining redshifts, some spectral classifications were obtained. Six sources were classified as AGNs in this way, and two as star-forming galaxies.

*x*.—If a source was detected by *Chandra* (Giacconi et al. 2002), then in a few cases we can use its hardness ratio (HR) to classify it (Rosati et al. 2002). All galaxies studied by Rosati et al. with HR $> 0.2$ are classified as type II AGNs, so here we classify all such galaxies as AGNs. Sources with HR $< -0.2$ are usually either a type I AGN or a star-forming galaxy, although a few type II AGNs also have this HR. Therefore, in cases in which the optical image precludes a type I AGN, we conclude that most such sources are likely to be star-forming galaxies, but this is far from an unambiguous classification. Three sources were classified as AGNs, and two were confirmed as star-forming galaxies on the basis of their X-ray properties.

In addition, we note that sources could arguably be classified as AGNs if their radio luminosity is $>10^{24}$ W Hz$^{-1}$, as all well-known galaxies at this radio luminosity are AGNs, but we have not done this since it preempts the possibility raised by Chapman et al. (2003b) and others that there may be superstarbursts with very high radio luminosities.

We also note that the above classification process can successfully identify AGNs but is very inefficient at classifying star-forming galaxies. Thus, nearly all our classifications are of AGNs. However, R. P. Norris et al. (2006, in preparation) have shown that a significant fraction of the remaining galaxies have a SED characteristic of star formation. This confirms the findings of previous radio surveys that find both AGNs and star formation–driven objects represented in such samples. However, we emphasize that these classifications are heavily biased in favor of AGNs and should not be used as an estimator of star formation/AGN activity.

### 3.5. *The Source Catalog*

The radio source catalog is presented in Table 6, with the following columns.

*Column* (*1*).—Source number. This is the internal designation of the source used within this paper.

*Column* (*2*).—Designation for this radio source. In the case of single-component sources, this is identical to the component name used in Table 4.

*Column* (*3*).—Component number(s) corresponding to Table 4.

*Column* (*4*).—Designated name of the SWIRE identification used in SWIRE Public Data Release 3. In cases in which the source does not appear in the Public Data Release 3 but did appear in the prerelease catalog, the source identification from the prerelease catalog is shown in brackets. A blank indicates there is no cataloged SWIRE source, but a source may still be present in the SWIRE image, in which case it is noted in the "Comments" column.

*Columns* (*5*) *and* (*6*).—Right ascension (J2000.0) and declination (J2000.0). In the case of a single component, this is the position of the radio source. In the case of a complex source, such as a radio double, this is the position of the host galaxy. In the latter case this is the optical position if one is available, or else an infrared position.

*Column* (*7*).—Total flux density at 20 cm (in millijanskys). This is the total integrated 20 cm flux of all components included in the source.

*Columns* (*8*)–(*12*).—Infrared fluxes measured at 3.6, 4.5, 5.8, 8, and 24 $\mu$m in microjanskys. These fluxes are optimized so that they are aperture extractions for point sources and extended (Kron) extractions for extended sources. A "$-1$" indicates that the source was undetected, and a blank indicates that the source was not observed or that its flux is not listed in the SWIRE catalog.

*Columns* (*13*)–(*17*).—SDSS $U/u'$, $g'$, $r'$, $I'$, and $z'$ aperture magnitudes for stellar sources, and integrated magnitudes for extended sources. All are in the Vega system. Filter characteristics are shown in Table 3. A "99" indicates that the source was undetected, and a blank indicates that the source was not observed.

*Column* (*18*).—Spectroscopic redshift. In most cases these have been measured by us as part of this program, as described in § 2.5. In some cases they are taken from other authors, in which case this is noted in the "Comments" column. To avoid ambiguity, photometric redshifts are not included here.

*Column* (*19*).—Type and accuracy of the radio-infrared identification, using the code listed in Table 5.

*Column* (*20*).—Classification (AGN/star formation) based on the criteria described in § 3.4.

*Column* (*21*).—Basis for the classification. The criterion used for the classification is given by the lower case letter: (a) morphology (i.e., double, triple, or core-jet radio source); (b) value of $q_{24\ \mu\mathrm{m}} = \log(S_{24\ \mu\mathrm{m}}/S_{20\ \mathrm{cm}})$; (c) classification taken from the literature; (s) based on spectroscopy presented in this paper; (x) based on X-ray HR given by Giacconi et al. (2002.)

*Column* (*22*).—Comments. "*M*-test" refers to the criterion for selecting double radio sources described by Magliocchetti et al. (1998), and "XIDnnn(mm)" indicates that the source was detected by *Chandra* (Giacconi et al. 2002) and is labeled XIDnnn, with HR mm, in their catalog. The terms *z*(x) give the reference for the redshift as follows: (a) this paper (ADROIT observations); (b) this paper (AAOmega observations); (c) Afonso et al. (2006); (d) Croom et al. (2001); (e) da Costa et al. (1998); (f) Vanzella et al. (2006); (g) Colless et al. (2001); (h) Le Fevre et al. (2004); (i) Loveday et al. (1996); (j) Cimatti et al. (2004); (k) Way et al. (2005); and (l) Lauberts & Valentijn (1989).

### 3.6. *A Representative Sample of Sources*

Here we present images of a small but representative sample of sources to illustrate the quality of the data and also to illustrate the issues that impact on source identification. In each case an image is shown in Figure 3 that shows the 20 cm radio contours (with the lowest contour generally set at 100 $\mu$Jy) overlaid on the 3.6 $\mu$m SWIRE images. References to the SED are all taken from R. P. Norris et al. (2006, in preparation).

#### 3.6.1. *The S323 Region*

Figure 3 (*top*) shows a region in which several types of objects are visible. S323 = ATCDFS J033117.00−275515.3 (C342, C346, and C348) is a classical triple radio galaxy, with a bright SWIRE galaxy coincident with its core. The *M*-test successfully identifies these three sources as associated. The morphology of this source (two bright radio lobes surrounding a bright SWIRE source) is unmistakable. Spectroscopy shows the host galaxy to lie at a redshift of 1.37, with the spectrum of a broad-line quasar.

To the north lies a single strong radio component (S331/C355 = ATCDFS J033124.89−275208.3) that is coincident with a reasonably bright SWIRE source, which is also visible at optical wavelengths. This source has $q_{24\ \mu\mathrm{m}} = \log(S_{24\ \mu\mathrm{m}}/S_{20\ \mathrm{cm}}) = -2.0$, indicating that within the host galaxy lies an AGN.

S291/C311 = ATCDFS J033055.63−275201.7 is an extended radio source, which may be a core/jet signifying an AGN. At its center is a SWIRE source with a measured spectroscopic redshift of 0.3382, and the SED of an elliptical galaxy.

S279/C298 = ATCDFS J033046.26−275517.5 is a single radio component coincident with a SWIRE source with the SED of a star-forming galaxy. The value of $q_{24\ \mu\mathrm{m}}$ for this galaxy is also consistent with the radio-FIR correlation, supporting its identification as a star-forming galaxy.

S287 = ATCDFS J033056.45−275508.0 is a linear arrangement of three radio components (C305, C307, and C312), which are remarkably symmetrical both in spacing and in flux density. These three components fall just below the *M*-test criterion because their flux densities are relatively low for the measured separation between them. The center component is coincident with a SWIRE galaxy with the SED of a star-forming galaxy, and a measured spectroscopic redshift of 0.8934, while the two outer components have no SWIRE identification, suggesting that this is a triple radio source. If this identification is correct, it suggests that an AGN is buried within a star-forming galaxy.

#### 3.6.2. *The S226 Galaxy*

C244/S226 = ATCDFS J032956.56−284632.6 is a diffuse 5 mJy radio source that is coincident with a bright barred spiral galaxy (ESO 418-G007) at $z = 0.037$, shown in Figure 3 (*middle*). In addition, 30″ away is a compact (but slightly resolved) 4 mJy radio source (C241/S223) that is coincident with a bright compact infrared object, which appears to lie at the end of one of the spiral arms of S226. We note that the *M*-test incorrectly classifies these two sources as a radio double.

#### 3.6.3. *The S440 Region*

Figure 3 (*bottom*) shows the region around this source and helps illustrate the nomenclature and conventions used in this paper. It also illustrates the shortcoming of the *M*-test when applied to deep surveys such as this.

Two nearby radio sources, S442 = ATCDFS J033229.84−274423.8 and S443 = ATCDFS J033229.97−274405.4, are clearly identified with bright SWIRE galaxies. These two sources were also observed by Afonso et al. (2006), who described them both as "flocculent" star-forming galaxies and measured a redshift for each of 0.076. They were also detected by *Chandra* (Giacconi et al. 2002) as XID 95 and XID 116, with HRs of $-0.7$ and $-0.156$, respectively, which, since their optical appearance precludes type 1 AGNs, suggests that they are star-forming galaxies (Rosati et al. 2002).

In the 3.6 $\mu$m IRAC image in Figure 3 there appears to be a weak bridge of emission connecting them, which was also noted by Giacconi et al. (2001), who classified them as "interacting."

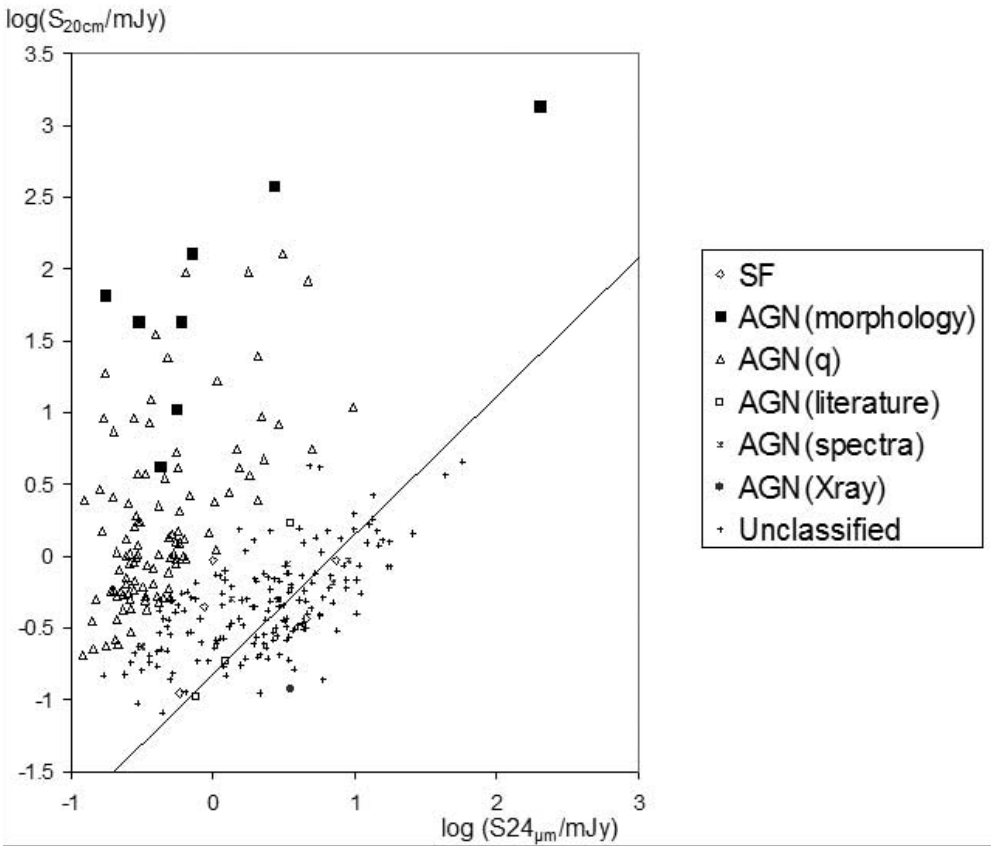


FIG. 4.—Observed 20 cm integrated flux plotted against SWIRE 24 $\mu$m flux for those sources in our sample that were also detected at 24 $\mu$m, classified according to the criteria discussed in § 3.4. The diagonal line shows the radio-FIR correlation $q_{24\,\mu\mathrm{m}} = \log(S_{24\,\mu\mathrm{m}}/S_{20\,\mathrm{cm}}) = 0.84$ suggested by the Appleton et al. data (2004).

The *M*-test classifies these two galaxies as a radio double, which is clearly incorrect.

Two other radio sources, identified here as components C473 and C476, were also observed by Afonso et al. (2006), who were unable to identify them at optical wavelengths. Here we also fail to find an identification at any of the SWIRE wavelengths. However, we note that they appear to be connected by a bridge of radio emission and that there is a bright SWIRE source (SWIRE3 J033228.79−274356.1) between them, and within the radio contours, and so we tentatively identify this as the host galaxy of a double radio source and designate the two components C473 and C476 as one radio source, S440 = ATCDFS J033228.79−274356.1. The *M*-test correctly classifies these two galaxies as a radio double. The central host galaxy is also detected by *Chandra* (XID 103) with HR $= -0.69$, suggesting this may be a type I AGN.

In addition, the *M*-test classifies C473 and C477, and C476 and C478, respectively, as radio doubles. It is clear that although the test has been demonstrated to work well at high flux densities, it is less successful at the flux densities observed here, because galaxies are far more likely to have nearby companions than at higher flux density levels. The reliability of classification is greatly increased by referring to data at other wavelengths, such as the *Spitzer* data.

## 4. DISCUSSION

### 4.1. *Starburst or AGN?*

It is well established (e.g., Dickey & Saltpeter 1984; de Jong et al. 1985) that in nearby galaxies dominated by star formation, the radio and FIR emission are strongly correlated, and Appleton et al. (2004) have shown that the correlation is still valid at high redshifts. Appleton et al. also showed that the correlation can be seen, albeit with a higher scatter, in plots of 24 $\mu$m (as opposed to FIR) flux against radio flux. B. J. Boyle et al. (2006, in preparation) have shown that the correlation is also present in stacked radio images down to microjansky levels.

Luminous radio galaxies and AGNs depart very strongly from the correlation (e.g., Sopp & Alexander 1991), making the correlation a good test for AGNs. A source that departs from the correlation is likely to be an AGN, but it cannot be concluded that a source that follows the correlation is not an AGN, because Roy et al. (1998) showed that most Seyfert galaxies also followed this correlation, suggesting that, despite the presence of an AGN, their radio luminosity is still dominated by star formation activity.

In Figure 4 we plot the observed integrated 20 cm radio flux against the observed 24 $\mu$m infrared flux for all our identified sources that have measured 24 $\mu$m fluxes. No *K*-correction has been performed here, or elsewhere in this paper, because redshifts and spectral shapes are generally too poorly known for this sample to do so with confidence. It is clear that all sources that have been classified as AGNs on the basis of their morphology depart very strongly from the correlation.

In the lower right of the diagram is a paucity of sources, and the sharp diagonal boundary between this space and the plotted points is close to the radio-FIR correlation. Our sample of sources clearly fails to follow the radio-FIR correlation, presumably because of the large numbers of radio-luminous AGNs in the sample. However, Figure 4 shows that the correlation is close to a lower bound to the value of $S_{20\,\mathrm{cm}}/S_{24\,\mu\mathrm{m}}$.

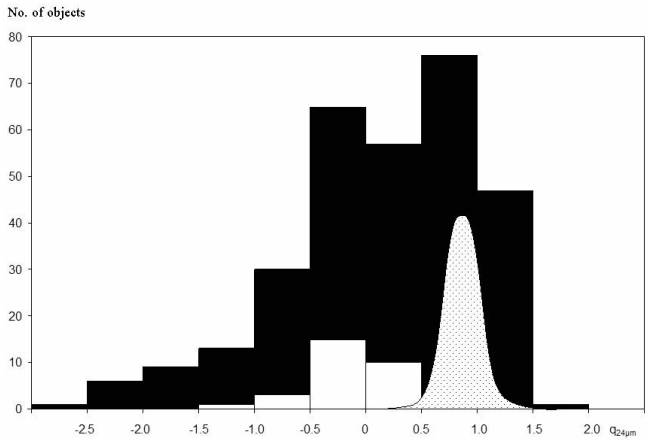


FIG. 5.—Distribution of values of $q_{24\,\mu m} = \log(S_{24\,\mu m}/S_{20\,cm})$. The black histogram represents the subsample of ATLAS sources for which 24 $\mu$m fluxes are available. The white histogram represents the upper limits derived by Higdon et al. (2005) for their sample of optically invisible radio sources, which are believed to be obscured AGNs. The Gaussian curve shows the approximate distribution of the sample of Appleton et al. (2004), which is dominated by star-forming galaxies.

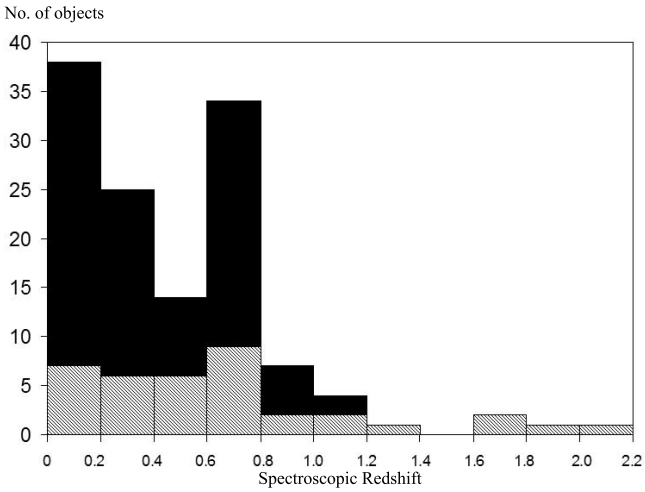


FIG. 6.—Histogram of spectroscopic redshifts for our sample. The upper curve (*black area*) shows the total for all objects, while the lower curve (*hatched area*) shows objects classified as AGNs.

This is more clearly demonstrated in Figure 5, which shows a histogram of $q_{24\,\mu m} = \log S_{24\,\mu m}/S_{20\,cm}$ for our sample and those of Higdon et al. (2005), which is dominated by obscured AGNs, and Appleton et al. (2004), which is dominated by star-forming galaxies (because their sample had been color-selected to maximize the number of star formation galaxies at around $z = 1$). The sharp cutoff on the right is caused by the significant absence of sources below the line in Figure 5, and is common to all such radio surveys. The tail (and possibly the peak) to the left of the plot indicate sources that are radio bright, and presumably driven by AGNs. Our sample clearly overlaps those of both Appleton et al. and Higdon et al. Presumably those overlapping the Appleton et al. curve are powered primarily by star formation activity, while those overlapping the Higdon curve are powered primarily by AGN activity. It should be noted that less than half of our radio sources are detected at 24 $\mu$m in the SWIRE Survey (although nearly all are detected at shorter wavelengths), and so there is a large undetected population of sources to the left of this plot.

Thus, although no quantitative conclusions can be drawn from this study, it is clear that our sample contains significant numbers of both AGNs and star-forming galaxies. This is supported by the X-ray and other indicators referred to in Table 6.

### 4.2. *Redshift Distribution*

In Figure 6 we show the distribution of spectroscopic redshifts for objects in our sample. Only seven of the sources in our sample are classified as star formation galaxies, which is too small to be usefully shown in this histogram, but we expect that most of the objects that have not been classified as AGNs are powered primarily by star formation.

The highest redshift object in our sample is at $z = 2.18$, and all objects at redshifts >1.2 are classified as AGNs. However, this is strongly influenced by selection effects, because only the optically brighter (typically $R < 22.5$) galaxies have so far had their redshifts measured, and AGNs tend to have more prominent emission lines. Photometric redshifts for this sample (R. P. Norris et al. 2006, in preparation) extend to significantly higher redshifts for both AGN and non-AGN galaxies.

Nevertheless, it is clear that the number of detected galaxies declines with redshift, as expected, with the exception of a pronounced maximum in both AGN and non-AGN galaxies at about $z = 0.7$, presumably due to large-scale structure, such as the clusters at $z = 0.66$ (Croom et al. 2001), and $z = 0.73$ (Gilli et al. 2003). We also note the flat tail extending to high redshifts, which consists entirely of AGNs.

### 4.3. *Infrared-Faint Radio Sources*

Richards et al. (1999) found that 20% of the microjansky radio sources in the Hubble Deep Field–North (HDF-N) had no counterpart brighter than $I = 25$. Further observations showed that several of these were very red, with $I - K > 4$. Norris et al. (2005) and Huynh et al. (2005) found a similar result in the HDF-S. For example, the strongest radio source in the HDF-S (ATHDFS J223258.5−603346) is extremely faint ($V = 27.05$) and red ($I - K = 3.45$), and is also unusually radio-loud [$\log(S20/I) = 3.74$]. However, whether the radio emission is being produced by star formation or by an AGN, we expect the dust that is apparently hiding the radio-producing activity to be bright at mid-IR wavelengths. Thus, we expected that all radio sources detected by ATLAS would appear in the SWIRE catalog.

Unexpectedly, we find that a small number of radio sources in our sample are not visible at any *Spitzer* wavelength. We denote this rare class of objects "infrared-faint radio sources" (IFRSs).

There are 22 such objects in our sample. While the weakest of these might be ascribed to statistically unusual noise peaks or imaging artifacts (although we have attempted to remove all such spurious sources), some of them are as strong as 5 mJy, and their reality is beyond question. Figure 7 shows two examples. In both cases, the sources are invisible in all *Spitzer* infrared wave bands (optical identification is limited by confusion), and so the only information on these sources comes from the radio.

Figure 8 shows a "stacked" IRAC image for all 22 IFRSs, which has been obtained by summing the individual 3.6 $\mu$m images centered on the 22 IFRS radio positions. We also show a stacked image of 3.6 $\mu$m images centered on the eight strongest IFRSs, in case the weaker ones are radio artifacts. No source is detected at the radio position at any *Spitzer* wave band in either of the stacked images, implying that the mean flux of these is at least a factor of $\sqrt{22}$ and $\sqrt{8}$, respectively, below the SWIRE sensitivity limit (Table 2). A similar result has been obtained at each of the other SWIRE bands. If the IFRSs simply represented a tail to the observed distribution of radio/infrared flux densities, then they would be expected to fall just below the SWIRE

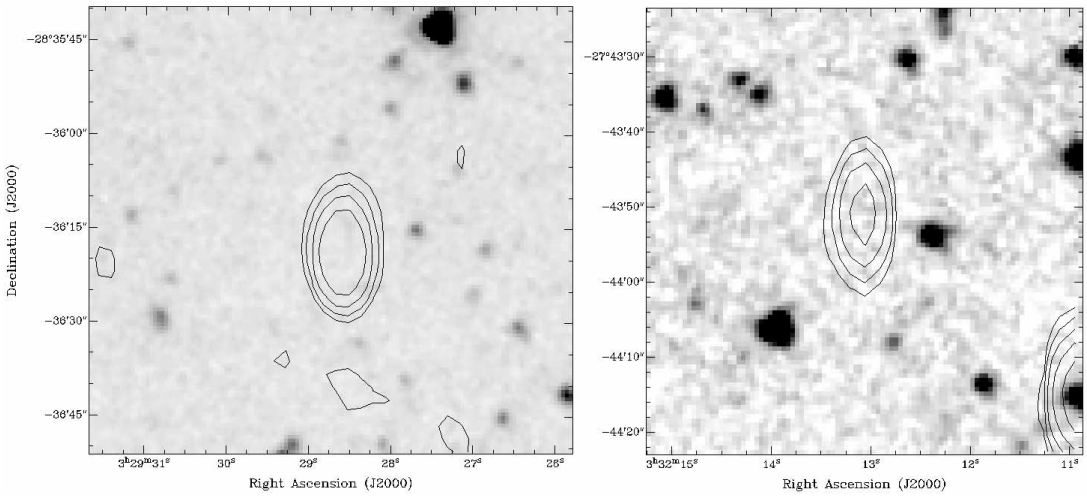


FIG. 7.—Two IFRSs, both of which are bright (∼6 mJy) at 20 cm but have no known infrared, optical, or X-ray counterpart.

sensitivity limit, and should appear in the stacked image. Their absence from the stacked image suggests either that the distribution of radio/infrared flux density ratios is bimodal or else that it has a tail extending to high values of that ratio.

Possible explanations for these sources include:

1. An AGN or star-forming galaxy so heavily obscured, or at such a high redshift, that all its dust emission is radiated at FIR wavelengths beyond 24 $\mu$m, and is thus undetectable by *Spitzer*. This model must also accommodate one case (S415) of a *Chandra* nondetection.
2. A starburst or AGN in a transitory phase in which electrons are producing radio emission but there is insufficient dust to produce detectable infrared emission.
3. A radio lobe from an unidentified radio source.
4. Some other exotic object, which may be Galactic.

Higdon et al. (2005) have identified a related class of sources that they denote "optically invisible radio sources" (OIRSs). The OIRSs they identify are 20 cm radio sources observed with the Very Large Array in the Bootes field that do not have an optical identification at *B*, *R*, or *I* bands. Most of the OIRSs also do not have a 24 $\mu$m detection at a sensitivity level of 0.3 mJy, which is similar to the SWIRE 24 $\mu$m sensitivity.

Assuming that the invisibility of both IFRSs and OIRSs is caused by dust extinction, the IFRSs have a more extreme selection criterion than OIRSs, in that we require no detection at any of the *Spitzer* bands, rather than at the shorter wavelengths required by OIRSs. Although most of the OIRS sources do not have 24 $\mu$m counterparts, the shorter SWIRE bands are generally more sensitive to both AGNs and star formation galaxies, and approximately half the radio sources presented in this paper do not have 24 $\mu$m counterparts. Thus, we expect the OIRSs and IFRSs to overlap, with the IFRSs generally being more extreme examples of OIRSs. IFRSs will be discussed at greater length by R. P. Norris et al. (2006, in preparation).

## 5. CONCLUSION

We have presented data for a sample of about 800 radio components in the CDF-S field, even though we are only about halfway through our radio survey of this region, primarily to facilitate

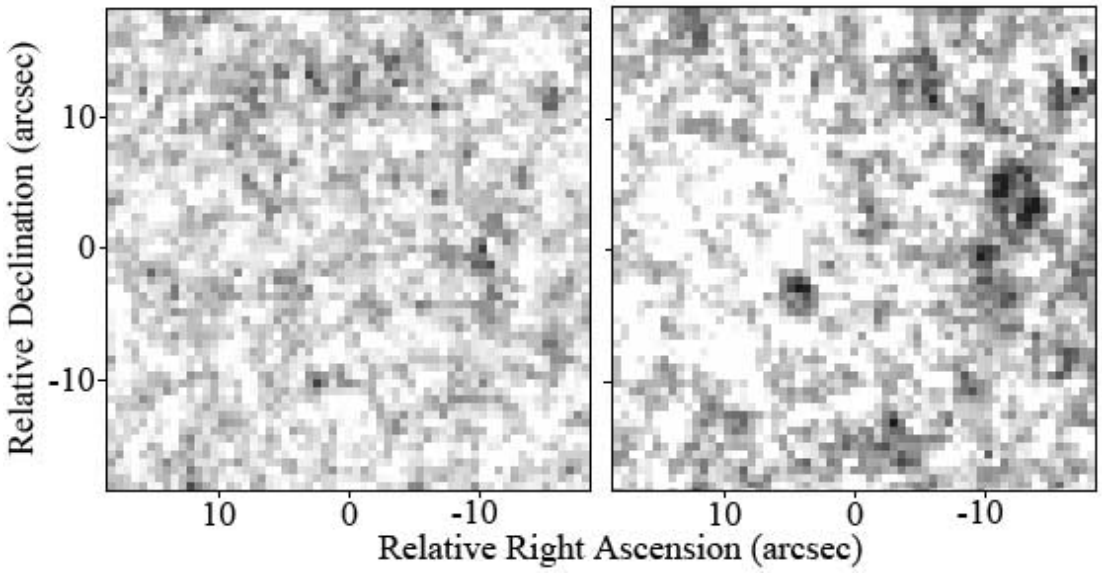


FIG. 8.—*Left*: Stacked 3.6 $\mu$m IRAC image of all 22 radio sources for which there is no infrared counterpart. *Right*: Stacked 3.6 $\mu$m IRAC image of the eight brightest radio sources for which there is no infrared counterpart. In both cases, the position of the radio source is at the center.

further work at other wavelengths. Because this sample is not yet statistically complete, we have restricted the discussion on the astrophysical implications. Nevertheless, we can draw some preliminary conclusions.

Some of the galaxies have radio data that show an unmistakable signature of an AGN, either because their radio–24 $\mu$m ratio departs from the expected correlation or because their radio morphology indicates classical radio doubles or triples. While some of these have also been identified as AGNs on the basis of optical or X-ray data, many have not, demonstrating the value of radio observations as a technique for identifying AGNs. In particular, some galaxies that we have classified as AGNs have not been detected by *Chandra*, and we note that other authors (Alonso-Herrero et al. 2006; Donley et al. 2005; Rigby et al. 2005) have also reported radio-selected AGNs that have not been detected by *Chandra*.

About half the ATLAS radio sources lie close to the radio-FIR correlation and are presumably driven primarily by star formation activity. Thus, the ATLAS radio sources include comparable numbers of both star-forming galaxies and AGNs. However, all galaxies with a measured redshift greater than 1.2 have been classified as AGNs, from which we conclude that, at the current level of sensitivity, star-forming galaxies are mainly confined to redshifts of less than about 1. We find no evidence for high-luminosity star-forming galaxies at $z > 1$, although we acknowledge that this may be partly attributed to the difficulty of measuring redshifts of galaxies other than AGNs at high redshifts.

We have also identified a class of radio sources, the infrared-faint radio sources, that are invisible at optical and infrared wavelengths. These objects are rare (a few per square degree at current sensitivity levels), and so can only be found in wide, deep surveys such as this. We expect to find more of these objects as we continue to increase the sensitivity of ATLAS by adding the observations that are planned over the next 1–2 years.

We thank Jim Condon for helpful comments on this paper. R. P. N. gratefully acknowledges "Visiting Scientist" support from the Spitzer Science Center, J. A. gratefully acknowledges support from the Science and Technology Foundation (Portugal) through research grant POCTI/CTE-AST/58027/2004, and I. R. S. acknowledges support from the Royal Society. The Australia Telescope Compact Array is part of the Australia Telescope, which is funded by the Commonwealth of Australia for operation as a National Facility managed by CSIRO. This research has made use of the NASA/IPAC Extragalactic Database, which is operated by the Jet Propulsion Laboratory, California Institute of Technology, under contract with the National Aeronautics and Space Administration. This research has also made use of the VizieR catalog access tool, CDS, Strasbourg, France.

REFERENCES

Afonso, J., Georgakakis, A., Almeida, C., Hopkins, A., Cram, L., Mobasher, B., & Sullivan, M. 2005, ApJ, 624, 135
Afonso, J., Mobasher, B., Koekemoer, A., Norris, R. P., & Cram, L. 2006, AJ, 131, 1216
Alonso-Herrero, A., et al. 2006, ApJ, 640, 167
Appleton, P. N., et al. 2004, ApJS, 154, 147
Bertin, E., & Arnouts, S. 1996, A&AS, 117, 393
Blain, A. W., Chapman, S. C., Smail, I., & Ivison, R. 2004, ApJ, 611, 725
Bondi, M., et al. 2003, A&A, 403, 857
Chapman, S. C., Blain, A. W., Ivison, R. J., & Smail, I. R. 2003a, Nature, 422, 695
Chapman, S. C., et al. 2003b, ApJ, 585, 57
Cimatti, A., et al. 2004, Nature, 430, 184
Colless, M., et al. 2001, MNRAS, 328, 1039
Condon, J. J. 1984, ApJ, 287, 461
———. 1997, PASP, 109, 166
Condon, J. J., Cotton, W. D., Greisen, E. W., Yin, Q. F., Perley, R. A., Taylor, G. B., & Broderick, J. J. 1998, AJ, 115, 1693
Condon, J. J., et al. 2003, AJ, 125, 2411
Croom, S. M., Warren, S. J., & Glazebrook, K. 2001, MNRAS, 328, 150
da Costa, L. N., et al. 1998, AJ, 116, 1
de Jong, T., Klein, U., Wielebinski, R., & Wunderlich, E. 1985, A&A, 147, L6
de Ruiter, H. R., Arp, H. C., & Willis, A. G. 1977, A&AS, 28, 211
Dickey, J. M., & Saltpeter, E. E. 1984, ApJ, 284, 461
Dole, H., et al. 2006, A&A, 451, 417
Donley, J. L., Rieke, G. H., Rigby, J. R., & Pérez-González, P. G. 2005, ApJ, 634, 169
Georgakakis, A., Mobasher, B., Cram, L., Hopkins, A., Lidman, C., & Rowan-Robinson, M. 1999, MNRAS, 306, 708
Giacconi, R., et al. 2001, ApJ, 551, 624
———. 2002, ApJS, 139, 369
Giavalisco, M., et al. 2004, ApJ, 600, L93
Gilli, R., et al. 2003, ApJ, 592, 721
Glazebrook, K., & Bland-Hawthorn, J. 2001, PASP, 113, 197
Higdon, J. L., et al. 2005, ApJ, 626, 58
Hopkins, A. M., Afonso, J., Chan, B., Cram, L. E., Georgakakis, A., & Mobasher, B. 2003, AJ, 125, 465
Huynh, M. T., Jackson, C. A., Norris, R. P., & Prandoni, I. 2005, AJ, 130, 1373
Koekemoer, A. M., Mobasher, B., & Norris, R. P. 2003, NewA Rev., 47, 391
Kron, R. G. 1980, ApJS, 43, 305
Lauberts, A., & Valentijn, E. A. 1989, The Surface Photometry Catalogue of the ESO-Uppsala Galaxies (Garching: ESO)
Le Fevre, O., et al. 2004, A&A, 428, 1043
Lonsdale, C. J., et al. 2003, PASP, 115, 897
Loveday, J., Peterson, B. A., Maddox, S. J., & Efstathiou, G. 1996, ApJS, 107, 201
Magliocchetti, M., Maddox, S. J., Lahav, O., & Wall, J. V. 1998, MNRAS, 300, 257
Magorrian, J., et al. 1998, AJ, 115, 2285
Miszalski, B., Shortridge, K., Saunders, W., Parker, Q. A., & Croom, S. M. 2006, MNRAS, in press
Norris, R. P., et al. 2005, AJ, 130, 1358
Reynolds, J. E. 1994, A Revised Flux Scale for the AT Compact Array (ATNF Int. Memo AT/39.3/040; Epping: ATNF)
Richards, E. A., Fomalont, E. B., Kellermann, K. I., Windhorst, R. A., Partridge, R. B., Cowie, L. L., & Barger, A. J. 1999, ApJ, 526, L73
Rigby, J. R., Rieke, G. H., Pérez-González, P. G., Donley, J. L., Alonso-Herrero, A., Huang, J.-S., Barmby, P., & Fazio, G. G. 2005, ApJ, 627, 134
Rosati, P., et al. 2002, ApJ, 566, 667
Roy, A. L., Norris, R. P., Kesteven, M. J., Troup, E. R., & Reynolds, J. E. 1998, MNRAS, 301, 1019
Sault, R. J., Teuben, P. J., & Wright, M. C. H. 1995, in ASP Conf. Ser. 77, Astronomical Data Analysis Software and Systems IV, ed. R. A. Shaw, H. E. Payne, & J. J. E. Hayes (San Francisco: ASP), 433
Sault, R. J., & Wieringa, M. H. 1994, A&AS, 108, 585
Sopp, H. M., & Alexander, P. 1991, MNRAS, 251, 14P
Stevens, J. A., et al. 2003, Nature, 425, 264
Vanzella, E., et al. 2006, A&A, 454, 423
Way, M. J., Quintana, H., Infante, L., Lambas, D. G., & Muriel, H. 2005, AJ, 130, 2012
Windhorst, R. A., Miley, G. K., Owen, F. N., Kron, R. G., & Koo, D. C. 1985, ApJ, 289, 494